

Innovative Silicosis and Pneumonia Classification: Leveraging Graph Transformer Post-hoc Modeling and Ensemble Techniques

Bao Q. Bui, Tien T.T. Nguyen, Duy M. Le, Cong Tran, and Cuong Pham

Abstract—This paper presents a comprehensive study on the classification and detection of Silicosis-related lung inflammation. Our main contributions include 1) the creation of a newly curated chest X-ray (CXR) image dataset named SVBCX that is tailored to the nuances of lung inflammation caused by distinct agents, providing a valuable resource for silicosis and pneumonia research community; and 2) we propose a novel deep-learning architecture that integrates graph transformer networks alongside a traditional deep neural network module for the effective classification of silicosis and pneumonia. Additionally, we employ the Balanced Cross-Entropy (BalCE) as a loss function to ensure more uniform learning across different classes, enhancing the model's ability to discern subtle differences in lung conditions. The proposed model architecture and loss function selection aim to improve the accuracy and reliability of inflammation detection, particularly in the context of Silicosis. Furthermore, our research explores the efficacy of an ensemble approach that combines the strengths of diverse model architectures. Experimental results on the constructed dataset demonstrate promising outcomes, showcasing substantial enhancements compared to baseline models. The ensemble of models achieves a macro-F1 score of 0.9749 and AUC ROC scores exceeding 0.99 for each class, underscoring the effectiveness of our approach in accurate and robust lung inflammation classification.

Index Terms—pneumonia detection, silicosis detection, lung disease classification, ensemble learning

I. INTRODUCTION

A. Background and Motivation

Pneumoconiosis is a collective term encompassing a range of lung disorders resulting from the inhalation of diverse dust types, such as coal dust, fine particles, and metal particles. The human respiratory system is unable to entirely expel these particles, causing their gradual buildup in the lungs and leading to inflammation and fibrosis of lung tissues. As these

Bao Q. Bui is with VinUniversity, Vinhomes Oceans Park, Gia Lam District, Hanoi 10000, Vietnam (e-mail: bao.bq@vinuni.edu.vn).

Tien T.T. Nguyen is with Thai Nguyen University, Thai Nguyen 24000, Vietnam. (e-mail: nguyenthientien@tnmc.edu.vn).

Duy M. Le is with Post & Telecommunication Institute of Technology in Hanoi, Vietnam. (e-mail: leminhduy131002@gmail.com).

Cong Tran is with Post & Telecommunication Institute of Technology in Hanoi 10000, Vietnam. (e-mail: congtt@ptit.edu.vn).

Cuong Pham is with Post & Telecommunication Institute of Technology in Hanoi 10000, Vietnam. (e-mail: cuongpv@ptit.edu.vn).

Bao Bui-Quoc and Tien T.T. Nguyen contributed equally to this work. Corresponding author: Cuong Pham.

dust varieties are specific to certain workplaces, they are categorized as occupational pneumoconiosis. Occupations with an elevated risk of developing occupational pneumoconiosis include roles in coal mines, metal mining (aluminum, iron, copper, etc.), stone quarrying, cutting, grinding, and related activities. Among the 28 occupational diseases covered by insurance in Vietnam, the prevalence of occupational pneumoconiosis, particularly silicosis, reached 74.40% by the end of 2011¹.

Silicosis, the oldest recognized occupational lung disease, results from inhaling minuscule particles of silicon dioxide, often in the form of crystalline silica such as quartz or silicate minerals attached to other components like talcum powder [1]. Individuals at the highest risk include those engaged in transporting or blasting rocks and sand (miners, quarry workers, stone cutters) or using abrasive materials containing silica (sand, glass manufacturers, foundries, gemstone workers, ceramics). Coal miners face the risk of developing mixed silicosis and occupational lung diseases [2], [3]. Over time, these silica particles accumulate in patients' lungs and airways, resulting in breathing difficulties, respiratory system weakening, and, in severe cases, potential fatality [4]. The typical manifestations of occupational silicosis comprise:

- Respiratory distress (the cardinal symptom of occupational silicosis)
- Cough
- Lower limb edema (edema in the lower limbs may manifest as the disease advances, precipitating circulatory complications)
- Thoracic discomfort (patients may experience pain or discomfort in the thoracic region)
- Fatigue and muscular debility.

Based on clinical symptoms, doctors need to conduct a thorough examination and perform several tests before diagnosing whether the patient has silicosis. This evaluation involves assessing the patient's breathing capacity both at rest and during physical activity, as well as gathering detailed information about their occupational history to assess potential exposure to silica dust. For individuals suspected of having

¹Ministry of Health Portal: https://moh.gov.vn/web/phong-chong-benh-nghe-nghiep/thong-tin-hoat-dong/-/asset_publisher/xjpQsFUZRw4q/content/benh-bui-phoi-nghe-nghiep-nguy-co-phong-va-tri?inheritRedirect=false

silicosis, doctors typically recommend the following specific diagnostic tests to ascertain the presence of silica particles in the lungs: ²

- **Chest X-rays (CXR) or lung CT scans** [5]–[7] enable the doctor to assess the condition and extent of lung damage to determine if the patient has the disease.
- **Lung function tests** to evaluate the respiratory ability of the lungs. This measurement is conducted through two separate tests: lung capacity measurement and diffusing capacity. The results will be used to gauge the degree of lung damage in the patient.
- **Bronchoscopy:** A small, flexible tube with a camera at the end is inserted through the mouth or nose into the trachea and lungs. Bronchoscopy helps obtain the clearest images of the lungs. Additionally, during the bronchoscopy procedure, the doctor can take additional tissue and fluid samples.
- **Sputum testing:** Mucus is collected from the patient’s throat for testing and analysis.
- **Lung biopsy surgery:** The doctor administers general anesthesia to perform chest surgery, extracting lung tissue samples from the patient for testing.

Imaging diagnosis, particularly CXR for exposed patients, is a commonly employed method. Furthermore, X-ray-based identification can be integrated into decision support systems, utilizing deep learning models to aid physicians/healthcare professionals in diagnosis and decision-making. Hence, it is crucial to construct a CXR image dataset inclusive of silicosis and design deep-learning models suitable for disease detection.

In this paper, our fundamental contributions are:

- We constructed a new CXR image dataset, named SVBCX, comprising three classes of lung inflammation corresponding to three different causative agents. The utilization of this dataset for training deep learning models for classification purposes will assist experts in detecting lung inflammation, particularly among workers exposed to crystalline silica dust.
- We propose a novel model architecture that integrates a Graph Transformer network Plugin (GTP) behind a deep neural network (DNN) module and incorporates Balanced Cross-Entropy (BalCE) for loss function selection. These designs are implemented to facilitate more uniform learning across data classes.
- The ensemble of models serves to amalgamate the strengths of each unique architecture. Experimental results on the SVBCX dataset showcase promising outcomes, demonstrating notable enhancements compared to baseline models.

B. Organization and Notations

The organization of the upcoming sections in the paper is outlined as follows. Initially, Section II provides a survey and review of relevant articles and methods related to this problem. Subsequently, in Section IV, we outline the problem and provide detailed explanations of the proposed methods,

TABLE I: Summary of notations

Notation	Description
\mathbf{x}_i	The i -th input RGB image in the training set
y_i^j	The probability for the i -th image to be in class j .
\mathcal{T}	The training dataset
N	Number of samples in the training dataset
\mathcal{X}	The input image space
\mathcal{Y}	The output label space
H, W	The height and width of an image
f_θ	The overall neural network with learnable parameter θ
\mathcal{F}_{θ_f}	The feature extractor network with learnable parameter θ_f
\mathcal{W}_{θ_w}	The classifier layer producing the logits with learnable parameter θ_w
\mathbf{v}	The feature representation of size d
\mathbf{z}	The logit vector with size 4

encompassing the GTP plugin architecture, the utilized loss function, and the approach to ensemble modeling. Finally, the dataset description and experimental results are presented in Section V, and Section VI concludes with a summary and discussion of the problem.

The notations that are used in this paper are summarized in Table I. These notations are formally defined in the following sections that describe our method and technical details.

II. RELATED WORK

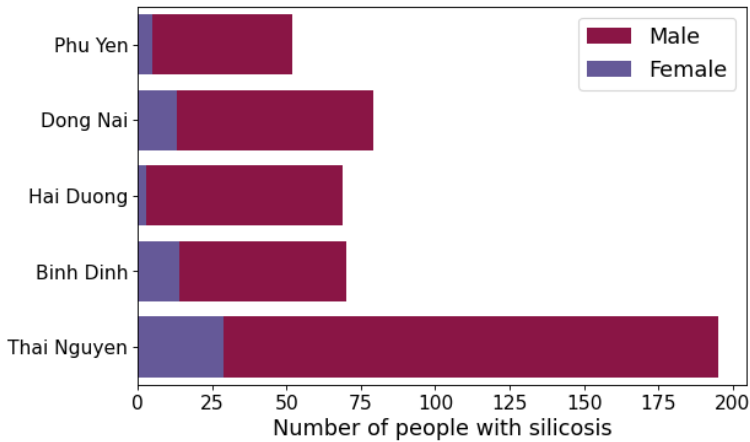
A. Radiologist-Guided Methods

CXR have been a mainstay in the diagnosis of lung diseases for over a century [8]. Traditionally, radiologists visually assess these images to identify specific patterns and abnormalities suggestive of various pulmonary conditions. This approach, while valuable, can be time-consuming and requires extensive training and experience. Additionally, the subjective nature of interpretation can lead to interobserver variability, where different radiologists may reach different conclusions when analyzing the same image [9].

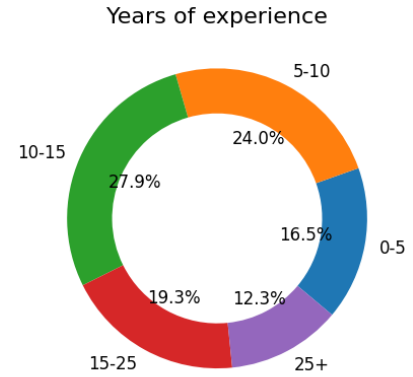
Furthermore, the increasing prevalence of lung diseases, coupled with the growing demand for efficient and accurate diagnosis, necessitates exploring alternative strategies to complement and potentially augment traditional methods. In this context, research efforts have focused on developing various computer-aided diagnostic (CAD) [10] systems to assist radiologists in interpreting CXR. These systems often employ image processing and analysis techniques to extract relevant features from the images and provide additional insights or decision support for improved diagnostic accuracy and efficiency.

Beyond CAD systems, other areas of research have explored alternative approaches for lung disease diagnosis using CXR. Some studies have investigated the potential of clinical decision support systems (CDSS) that integrate patient history and other clinical data with CXR findings to provide comprehensive recommendations for diagnosis and management [11].

²<https://tamanhhospital.vn/bui-phi-silic/>



(a) Statistics by gender and location.



(b) Statistics by years of experience.

Fig. 1: Statistics of individuals diagnosed with silicosis pneumonia.

Additionally, research has delved into the development of standardized reporting systems for CXR, aiming to improve the consistency and accuracy of interpretations across different healthcare providers [12]. These efforts contribute to reducing interobserver variability and enhancing communication between radiologists and other clinicians.

B. Traditional machine learning methods

Detecting lung diseases from CXR images in general, and pneumonia in particular, has been a challenging task, primarily due to the limited availability of annotated data [13], [14]. Traditional machine-learning methods have been extensively explored to tackle this issue. Chandra et al. [15] concentrated on lung region segmentation and extracted eight statistical features. They employed classifiers such as multi-layer perceptron (MLP), random forest, sequential minimal optimization (SMO), classification via regression, and logistic regression. Demonstrating promise, their method achieved a notable 95.39% accuracy using MLP on a dataset of 412 images. Kuo et al. [16] utilized 11 features for pneumonia detection in schizophrenia patients, achieving an impressive 94.5% accuracy with a decision tree classifier. Yue et al. [17] applied 6 features on chest CT scans, reaching a peak AUC of 97%. However, these methods faced limitations in handling multi-dimensional X-ray images or complex medical data, often exhibiting reduced flexibility and limited adaptability.

C. Deep learning based methods

The landscape of medical image analysis has witnessed a transformative shift from traditional machine learning approaches to the dominance of deep learning methods. Unlike machine learning algorithms that rely on handcrafted features for classification or segmentation [18], [19], deep learning techniques enable end-to-end classification, automatically extracting relevant features from input data [20], [21]. Convolutional Neural Networks (CNNs), especially, have become a cornerstone for image data classification due to their ability to

automatically extract translationally invariant features through convolution processes.

Sharma et al. [22] and Stephen et al. [23] exemplify this paradigm shift by devising simple CNN architectures for the classification of pneumonic CXR images. Despite the scarcity of data, they employed data augmentation to enhance model performance. However, the limitations of data augmentation in providing substantial new information to boost CNN performance became evident. Rajpukar et al. [24] showcased a groundbreaking application of CNNs with CheXNet, a 121-layer CNN for analyzing lung diseases, highlighting challenges such as a 76.8% f1-score and suspecting the impact of unavailable patient history on model performance. This model not only predicts lung diseases but also provides a heat map indicating the region of interest in X-rays. Subsequent research [25] extensively explored the utilization of state-of-the-art CNN architectures for pneumothorax detection, achieving notable success with an AUC of 0.75. The introduction of Darknet by Ozturk et al. [26] marked a new method for automatic COVID-19 detection using unprocessed chest X-ray images. Their approach achieved high accuracy in binary and multi-class classifications. AIMamlook et al. [27] proposed a comprehensive model combining seven machine learning models with well-known CNN models, achieving an impressive overall accuracy of 98.46%. These studies underscore the pivotal role of CNNs in advancing medical image analysis, especially in the context of critical respiratory conditions.

To address dependencies on dataset sources and enhance prediction robustness, Janizek et al. [28] introduced a framework based on adversarial optimization, achieving commendable AUC scores in both source and target domains. Similarly, Zhang et al. Authors in [29] proposed a confidence-aware module for anomaly detection in lung X-ray images, framing the task as a one-class problem and achieving an 83.61% AUC score. Tuncer et al. [30] applied a machine learning-based method with fuzzy tree transformation and multi-kernel local binary pattern, showcasing a 97.01% accuracy rate on a small dataset of COVID-19 and pneumonia samples.

Recognizing the data scarcity challenge in biomedical image

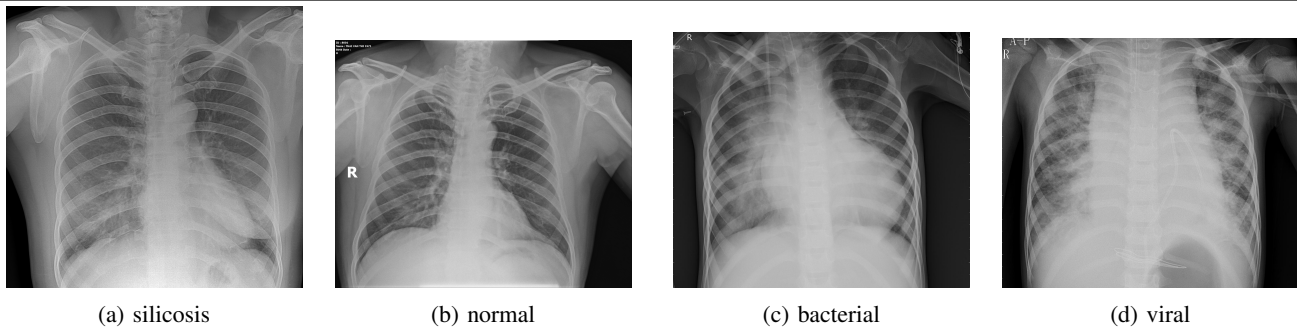


Fig. 2: Sample images corresponding to four classification categories.

classification, transfer learning emerges as a frequently employed approach. Rahman et al. [31], Liang et al. [32], Ibrahim et al. [33], and Zubair et al. [34] contributed to this trend, applying purely transfer learning approaches where different CNN models pre-trained on ImageNet data are fine-tuned for pneumonia classification. This transition from traditional machine learning to deep learning reflects a significant stride in addressing complex medical image analysis tasks. Overall, the integration of deep learning, particularly CNNs, has revolutionized medical image analysis, surpassing the limitations of traditional machine learning algorithms. This evolution is evident in the success of CNN-based models for various lung diseases, emphasizing their robust feature learning capabilities and superior performance in classification tasks.

III. BENCHMARK DATASET

In this section, we introduce our newly collected dataset named SVBCX, including four classes termed Silicosis, Viral, and Bacterial Chest X-ray Dataset, comprising images depicting lung diseases such as silicosis, viral, and bacterial infections. In the following, we elaborate on the dataset's collection and processing procedures.

A. Data collection

The research team opted for a sample of 2,089 laborers directly involved in production activities and consistently exposed to silica dust in different locations in Viet Nam, such as Thai Nguyen (metalworking profession), Hai Duong (cement production), Binh Dinh, Phu Yen (granite mining), and Dong Nai (brick manufacturing). The minimum requirement for inclusion was a work duration of at least 1 year at the time of data collection. Specifically, those diagnosed with silicosis were treated at the National Lung Hospital for a duration of 1 year, spanning from June 1, 2019, to May 31, 2020. The selection criteria encompassed all silicosis patients admitted to the Occupational Lung Diseases Department of the National Lung Hospital, possessing X-ray images and results of 35 x 43 cm lung dust X-ray films following the ILO 2000 standard.

Among the collected data, 535 cases have been diagnosed with silicosis. Figure 1a illustrates the distribution of patients by gender and sampling location across the aforementioned 5 provinces. Owing to the dominance of male laborers, the proportion of male patients is notably higher. Moreover, Thai Nguyen province currently records the highest number of

patients nationwide. Analyzing the pie chart in Figure 1b on years of employment suggests that longer tenure correlates with an increased risk of contracting the disease. The lower incidence among individuals aged 15-20 and 25+ can be attributed to the smaller population within these age groups with substantial work experience.

B. Data processing

The collected data includes files in *.dcm* format, which can be visualized in a human-friendly manner using specialized software such as MicroDicom³ or RadiAnt⁴, among others. Nevertheless, employing this approach for viewing and saving data as *.jpg*/*.png* is both time-consuming and labor-intensive. Hence, we adopt certain transformation steps using Python code to consistently and automatically convert and store images in *.jpg* format. The resultant dataset consists of 2005 images, with 445 cases depicting silicosis lung disease, while the remaining 1560 cases showcase images of individuals without the disease.

Alongside the aforementioned dataset, we additionally incorporate data from [35]. Within the three classes of this dataset, we utilize 2772 images from the bacterial class and 1493 images from the viral class. These two categories correspond to distinct disease-causing agents, which are bacteria and viruses. The inclusion of these two classes in the overall dataset for the classification model aids the system in distinguishing between different types of pneumonia and their respective causative agents. The illustration in Figure 2 depicts examples of images corresponding to each category within the SVBCX dataset. This discrimination enables the system to make informed decisions for subsequent actions in patient care.

IV. PROPOSED METHOD

In this Section, we provide a comprehensive overview of the proposed approach. Initially, we delineate the problem formulation in IV-A. Following that, in IV-B, we present the GTP architecture in conjunction with traditional classification models. The selection and rationale behind our chosen loss functions are elaborated in Section IV-C. Lastly, IV-D delves into the techniques employed for ensemble modeling.

³<https://www.microdicom.com/>

⁴<https://www.radiantviewer.com/>

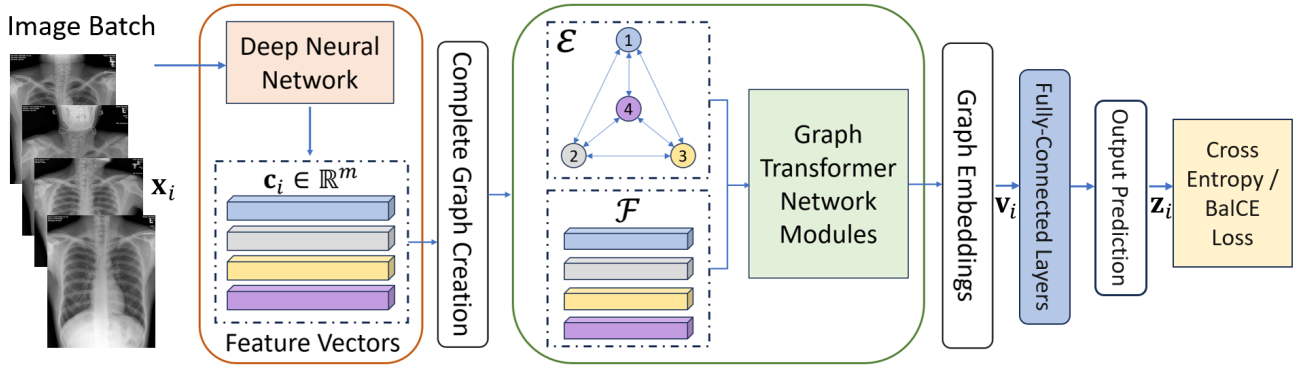


Fig. 3: An overview of Graph Transformer Post-hoc architecture design.

A. Problem formulation

The primary objective of this article is to develop and assess advanced deep learning models capable of learning from CXR images with a notable level of similarity among them, particularly in the context of fine-grained images. The models aim to proficiently classify three distinct types of pneumonia, each linked to a specific disease-causing agent. Specifically, silicosis is attributed to various metal dust, specifically silica dust, viral pneumonia is induced by viruses, and bacterial pneumonia resulting from bacterial infection.

We are provided with a training dataset $\mathcal{T} = \{(\mathbf{x}_i, \mathbf{y}_i)\}_{i=1}^N$ sampled from an unknown joint data distribution defined on $\mathcal{X} \times \mathcal{Y}$, where $\mathcal{X} \subset \mathbb{R}^{3 \times H \times W}$ and $\mathcal{Y} \subset \{0, 1\}^4$ represent the input image space and the output label space, respectively (with H and W indicating the height and width of an image in \mathcal{X}). Specifically, in this context, \mathbf{y}_i is a one-hot classification vector, where each position sequentially denotes the probability of the image \mathbf{x}_i belonging to one of the four classes: unseen, silicosis, bacterial, and viral.

Our objective is to train a model f with parameters θ , $f_\theta : \mathcal{X} \rightarrow \mathcal{Y}$, which maps each input image \mathbf{x}_i to an output vector \mathbf{y}_i in a way that minimizes the loss function across the entire training set \mathcal{T} .

In the context of network architecture, particularly concerning the function f , it involves: the encoder extracting the feature representation $\mathbf{v} := \mathcal{F}(\mathbf{x} | \theta_f) \in \mathbb{R}^d$, and the classifier producing the logits $\mathbf{z} := \mathcal{W}(\mathbf{v} | \theta_w) \in \mathbb{R}^4$, with d representing the feature dimension. In the subsequent two sections, we introduce an additional design option for \mathcal{F} and the choice of a loss function that utilizes the logits \mathbf{z} as an input.

B. Graph transformer Post-Hoc design

One of the key challenges in the field of medical image classification, particularly in the context of categorizing CXR images related to pneumonia, lies in the presence of class imbalance [36] and subtle distinctions within the image data. When there is substantial similarity among images, as is common in CXR datasets, traditional deep neural network (DNN) models encounter difficulties and are susceptible to confusion during classification due to closely related features in the embedding space. Additionally, the issue of data imbalance

worsens the aforementioned challenge, as the model tends to exhibit bias toward classes with a larger amount of data.

To enhance the learning balance between classes and improve the model’s understanding of complex CXR image relationships, we design an innovative structure for \mathcal{F} . This comprises a deep neural network Deep Neural Network (DNN) encoder for producing feature vectors \mathbf{c} . These vectors are subsequently organized into a complete graph and fed into a Graph Neural Network (GNN) model, specifically a Graph Transformer Network (GTN) [37], to obtain the final embeddings \mathbf{v} . Figure 3 illustrates the workflow of the GTP design, in which the GTN encoder can be considered a post-hoc plug-in.

Establishing connections between features in a batch, based on the layers of the GTN, serves to facilitate the grouping of elements belonging to the same class while simultaneously improving the separation between clusters of different classes. This approach, to some extent, addresses the challenge of data similarity. Experimental results illustrate that this architectural design “focuses” on classes with fewer instances, thereby alleviating the problem of data imbalance. In this part, a detailed exploration of the graph transformer post-hoc architecture will be provided.

DNN encoder. This encoder is commonly employed in any DNN-based image classification approach. For a training batch $\{\mathbf{x}_i, \mathbf{y}_i\}_{i=1}^b$ with a batch size of b , embeddings $\mathbf{c}_{i=1}^b$ are extracted from the input images batch.

GTN encoder. We denote a fully connected graph $\mathcal{G} = (\mathcal{V}, \mathcal{E}, \mathcal{F})$, where \mathcal{V} represents the set of images in each batch, i.e., $|\mathcal{V}| = b$, $\mathcal{E} = \{\mathbf{e}_{ij}\}_{i,j=1,\overline{b}}$ is the set of edges connecting images, and $\mathcal{F} = \{\mathbf{c}_1, \mathbf{c}_2, \dots, \mathbf{c}_b\}$ is the node features in the graph. We note that the edge weights \mathbf{e}_{ij} are learnable parameters, dynamically adjusted according to training data.

Firstly, the GTN module utilizes attention mechanisms to process information within the graph and enable the model to learn how vertices and edges interact. For each source node i , we compute the message aggregation from every other target node $j \in \mathcal{N}(i)$, with $\mathcal{N}(i)$ is the set of all vertices in the graph except i :

$$\hat{\mathbf{c}}_i = \sum_{j \in \mathcal{N}(i)} \alpha_{i,j} (\mathbf{W}_v \mathbf{c}_j + \mathbf{W}_e \mathbf{e}_{ij}). \quad (1)$$

Note that from now on, we denote \mathbf{W}_* as trainable parameters of the network. \mathbf{W}_v and \mathbf{W}_e are parameters for processing vertex and edge embeddings, respectively. The attention coefficients $\alpha_{i,j}$ are computed via multi-head dot product attention:

$$\alpha_{i,j} = \text{softmax} \left(\frac{(\mathbf{W}_q \mathbf{c}_i)^\top (\mathbf{W}_k \mathbf{c}_j + \mathbf{W}_e \mathbf{e}_{ij})}{\sqrt{d}} \right), \quad (2)$$

where \mathbf{W}_k and \mathbf{W}_q are parameters to compute the key and query of the attention module. We then combine aggregation and skip information as the following equation:

$$\mathbf{c}'_i = \beta_i \mathbf{r}_i + (1 - \beta_i) \hat{\mathbf{c}}_i \quad (3)$$

Using a gated residual connection, as outlined in Equation 4, to avoid over smoothing in our model:

$$\begin{aligned} \mathbf{r}_i &= \mathbf{W}_r \mathbf{c}_i \\ \beta_i &= \text{sigmoid}(\mathbf{W}_g [\hat{\mathbf{c}}_i; \mathbf{r}_i; \hat{\mathbf{c}}_i - \mathbf{r}_i]) \end{aligned} \quad (4)$$

Here, \mathbf{r}_i represents a residual connection using the residual parameter \mathbf{W}_r and a gated function β_i with gated weight \mathbf{W}_g .

In the end, the feature \mathbf{c}'_i acquired after traversing the TransformerConv layer will be subject to transformation via the fully connected layer to yield an d -dimensional feature vector, subsequently undergoing normalization using BatchNorm.

$$\mathbf{v}_i = \text{BatchNorm}(\text{Linear}(\mathbf{c}'_i)) \quad (5)$$

C. Loss functions

In our experiments, we observed that using the conventional Cross-Entropy loss function could lead models to be biased towards "easily recognizable" classes, such as normal classes in the case of CXR without abnormalities. This resulted in higher accuracy scores for these classes compared to others. Therefore, we introduced the option of using the BalCE [38] loss function to facilitate the model in attaining a more equitable learning process, mitigating this bias concern. Take into account the standard softmax operation and cross-entropy loss corresponding to class k ($k = \overline{0, 3}$):

$$\begin{aligned} \mathcal{L}_{\text{CE}} \left(\mathcal{W}(\mathcal{F}(\mathbf{x} | \theta_f) | \theta_w), k \right) \\ = -\log(p(k | \mathbf{x}; \theta_f, \theta_w)) = -\log \left[\frac{e^{\mathbf{z}_k}}{\sum_{j=1}^4 e^{\mathbf{z}_j}} \right]. \end{aligned} \quad (6)$$

When considering the class instance number n_k in the softmax function, we obtain the balanced cross-entropy loss:

$$\begin{aligned} \mathcal{L}_{\text{Bal-CE}} \left(\mathcal{W}(\mathcal{F}(\mathbf{x} | \theta_f) | \theta_w), k \right) \\ = -\log \left[\frac{n_k e^{\mathbf{z}_k}}{\sum_{j=1}^4 n_j e^{\mathbf{z}_j}} \right]. \end{aligned} \quad (7)$$

The two losses have a common objective of classification and are employed in the experiments described in the subsequent section.

TABLE II: Data statistics for the training and testing sets.

	Silicosis	Normal	Bacterial	Viral
Train	428	1244	2218	1195
Test	107	310	554	298

D. Ensemble of models

In tasks involving classification, particularly in medical image classification like Chest X-rays, where images exhibit high similarity, achieving consistently high scores across all disease labels is difficult for a singular model. Therefore, in this subsection, we present some simple yet effective ensemble techniques that combine models to leverage the strengths of each model and produce the best possible results.

Assume we have m distinct neural network models f^1, f^2, \dots, f^m , all trained on the training dataset. In the case of the max voting approach [39], predictions from each model are regarded as individual 'votes', and the ultimate prediction is determined by the most prevalent prediction among the models.

The Weighted Average method also involves predictions from multiple models, with each model assigned a weight proportional to its significance. However, in the final decision step, the weighted average of all selected model predictions is taken into account.

$$\text{pred}_{final} = \sum_{i=1}^m f^i(\mathbf{x}) * w^i \quad (8)$$

When all weights w^i are identical, the Averaging technique is employed.

V. EXPERIMENTS

A. Dataset statistics

In experiments conducted in this section, we employ the SVBCX dataset outlined in Section III, detailed in Table II. The dataset illustrates the distribution of various lung diseases, such as Silicosis, Normal, Bacterial, and Viral, within the datasets. The allocation ratio between the training and testing sets is 4:1, ensuring balanced proportions for subsequent analyses and model evaluations.

B. Experimental settings

1) *Implementation details:* We conduct all experiments using an NVIDIA Tesla T4 GPU with 15GB of RAM. Initially, we resize all input images to 224×224 pixels. During training, we apply simple data augmentation techniques such as RandomHorizontalFlip⁵ and RandomRotation⁶. The models are fine-tuned for 50 epochs with a batch size of 32 for all architectures. We adopt the Rectified Adam optimizer with a default epsilon value of 1e-8 and the initial learning rate is set to 1e-5.

⁵<https://pytorch.org/vision/0.17/generated/torchvision.transforms.RandomHorizontalFlip.html>

⁶<https://pytorch.org/vision/main/generated/torchvision.transforms.RandomRotation.html>

Regarding the network architectures in this experiment, we select three popular deep learning models: MobileNet [40], DenseNet [41], and SwinTransformer [42], along with three corresponding post-hoc plugin versions denoted as MobileNet-GTP, DenseNet-GTP, and SwinTransformer-GTP. For the graph transformer post-hoc architectures, the DNN encoder is trained using pre-trained weights from the ImageNet1K dataset. The GNN encoder integrates four graph transformer blocks in total. The first block transforms the output features of the base encoder into embeddings with a size of 1024. The remaining three blocks further transforms the features to ensure a consistent dimension of 1024 for the final embeddings across all six network models.

2) *Evaluation metrics*: We adopt the Macro-F1 and AUC-ROC scores as the main evaluation metrics for the silicosis classification problem.

Macro-F1 combines precision and recall to provide a single score that represents the overall performance of a classification model. It is particularly useful when dealing with imbalanced datasets. In the specific case of the problem discussed in this paper, the Macro-F1 formula is calculated as follows:

$$\text{Macro-F1} = \frac{1}{4} \sum_{i=1}^4 \frac{2 \times R_i \times P_i}{R_i + P_i}, \quad (9)$$

where P_i and R_i denote precision and recall, respectively, for class i in a multi-class classification scenario.

AUC-ROC. In this article, we calculate the AUC-ROC (Area Under the Receiver Operating Characteristic curve) for each of the 4 classes through a one-vs-all approach. Here, one class is designated as the positive class, and the remaining classes are grouped as the negative class. The AUC-ROC for each class is then determined using the same formula employed in binary classification problems, relying on the True Positive Rate and False Positive Rate.

C. Experimental results

In this section, our experiments are conducted to address the following research questions (RQs):

- 1) RQ1: How does the use of the CE loss function or Bal-CE impact the model's performance?
- 2) RQ2: What are the characteristics and effects of the architecture with GTP compared to a conventional DNN design on the SVBCX dataset?
- 3) RQ3: Does ensembling models leverage the capabilities of individual models, and what are the resulting outcomes?
- 4) RQ4: In classification problems, particularly in medical image processing, how do ensemble models fare when assessed using the Confusion Matrix, a pivotal metric?
- 5) RQ5: How do feature learning models perform, and what insights can be gained from their visualization and analysis of the data?
- 6) RQ6: How does the performance of the proposed model in classifying diseases compare to that of expert radiologists?

TABLE III: The result table of the models with accuracy under two loss function choices during training, namely Cross Entropy (CE) and Balanced Cross Entropy (Bal-CE).

Model	Silicosis	Normal	Bacterial	Viral
\mathcal{L}_{CE}				
MobileNet_V3_small	71.96	97.10	85.74	71.48
MobileNet_V3_small-GTP	74.77	93.87	84.84	72.15
$\mathcal{L}_{\text{Bal-CE}}$				
MobileNet_V3_small	72.03	95.16	76.17	83.89
MobileNet_V3_small-GTP	79.44	84.83	78.45	85.77

1) *The influence of different loss function types on model performance (RQ1)*: This experimental part demonstrates the performance accuracy of two models, MobileNet_V3_small and MobileNet_V3_small-GTP, across different lung disease classes (Silicosis, Normal, Bacterial, and Viral). Both models are trained using different loss functions: cross-entropy loss (\mathcal{L}_{CE}) and balanced cross-entropy loss ($\mathcal{L}_{\text{Bal-CE}}$). The comparison results for the four obtained models are presented in Table III. In both cases of loss functions, it is noted that the GTP architecture consistently outperforms in the Silicosis and Viral classes, while showing lower accuracy in the normal class. This implies that both models exhibit a greater focus on these two classes. Specifically, the inclusion of the $\mathcal{L}_{\text{Bal-CE}}$ loss amplifies this trend, leading to an accuracy improvement of over 7% compared to MobileNet_V3_small when using CE. These results indicate that the choice of loss function and model architecture significantly influences the model's ability to learn and classify specific classes. Each model has a tendency to prioritize certain classes, and the combination of these models is expected to harness their strengths for optimal overall performance.

2) *Comparison between the GTP model and the conventional DNN architecture (RQ2)*: We conduct experiments utilizing traditional DNN models employing the CE loss function and GTP models with the Bal-CE loss function. The outcomes were assessed using two above-mentioned metrics, Macro-F1 and AUC ROC (for each classification class).

The results presented in Table IV indicate that, in most instances, the incorporation of GTP into the DNN model does not consistently lead to higher Macro-F1 scores. To illustrate, MobileNet_V3_small-GTP exhibits a Macro-F1 0.02 points lower than its non-GTP counterpart. A higher Macro-F1 suggests that the DNN models with CE achieve a better balance between accuracy and recall across all classes, although the use of Bal-CE is supposed to bring about this "balance". In the context of this dataset, opting for the Bal-CE loss function alongside the GTP architecture significantly influences the model's ability to focus more accurately on the silicosis and viral classes, as demonstrated in RQ1.

Concerning the AUC ROC score, all scores surpassing 0.9 generally signify excellent discrimination performance in a classification model. When comparing models with and without the "-GTP" suffix, performance variations emerge. For in-

TABLE IV: A summary table of model results with two evaluation metrics, macro-F1 and AUC ROC (where rows in cyan correspond to models with the proposed GTP architecture).

Model	Macro-F1	AUC ROC			
		Silicosis	Normal	Bacterial	Viral
MobileNet_V3_small	0.8210	0.9768	0.9903	0.9342	0.9103
MobileNet_V3_small-GTP	0.8015	0.9505	0.9840	0.9455	0.9257
DenseNet201	0.8368	0.9557	0.9891	0.9385	0.9122
DenseNet201-GTP	0.8317	0.9512	0.9902	0.9493	0.9283
Swin_V2_b	0.8410	0.9722	0.9884	0.9633	0.9499
Swin_V2_b-GTP	0.8406	0.9749	0.9897	0.9576	0.9352
Max voting 3 DNNs	0.8808	0.9936	0.9973	0.9837	0.9777
Averaging 3 DNNs	0.9306	0.9985	0.9994	0.9928	0.9902
Max voting 3 GTPs	0.9164	0.9910	0.9968	0.9850	0.9793
Averaging 3 GTPs	0.9214	0.9903	0.9962	0.9869	0.9821
Max voting 6 models	0.9617	0.9969	0.9987	0.9950	0.9932
Averaging 6 models	0.9749	0.9973	0.9989	0.9973	0.9964

stance, MobileNet_V3_small-GTP displays slightly lower AUC ROC scores compared to its non-GTP counterpart. However, this trend is not consistent, as evidenced in DenseNet201 and DenseNet201-GTP.

In summary, each model type possesses unique advantages and may complement the other, suggesting that their combination holds the potential to yield favorable results.

3) Effectiveness of model ensembling (RQ3): To synthesize and leverage the strengths of each model type, we simply apply two hard voting techniques: max voting and averaging [39]. The three model groups selected for the ensemble include three DNNs, three GTP models, and finally, a combination of all six.

The ensemble models in Table IV consistently demonstrate superior results across all metrics compared to individual models. Specifically, with both ensemble methods, averaging consistently outperforms. This can be partially explained as follows: Averaging can mitigate the impact of "noise" predictions from some inaccurate models by averaging them out with accurate predictions from other models. Meanwhile, Max voting may prove more effective when some models are independent and high-performing, where majority voting results in elevated accuracy. As observed in the previous sections, each individual model has its own strengths, and no single model outperforms all others. Therefore, averaging them together synthesizes better and yields higher results.

While individual models under the GTP architecture tend to yield slightly lower macro-F1 scores, the ensemble of 3 GTPs outperforms 3 DNNs in scenarios like max voting, as observed.

In summary, the optimal results emerge from combining all

six models through averaging.

4) The ability of models to classify through the confusion matrix (RQ4): The confusion matrix is a valuable tool for evaluating a model's effectiveness in classification tasks, offering a comprehensive perspective on its performance across specific classes. In medical contexts, precise assessment of diagnostic accuracy is paramount, and metrics derived from the confusion matrix enable detailed and meaningful measurement of the model's performance.

The confusion matrices are formulated using 6 ensemble scenarios. As illustrated in Figure 4, one can see that in all instances, confusion only arises between two pairs: silicosis - normal and bacterial - viral (illustrated by both False Positive and False Negative values being zero for silicosis with bacterial or viral, for instance). In terms of techniques, employing an average with 3 GTPs yields the highest True Positive rate for silicosis, while averaging across 6 models surpasses other scenarios for the remaining three classes.

5) Visual analysis (RQ5): In our paper, we utilize Grad-CAM [43] to examine the chosen DenseNet201-GTP models. As depicted in Figure 5, the four generated samples, representing distinct classification classes, exhibit a heatmap primarily centered on the lung region in the X-ray images. Although Grad-CAM's data visualization technique may not completely reveal the model's learning mechanism, these instances imply that the model has, to a certain degree, acquired accurate knowledge regarding the content of the image data in the training set, specifically the lung region.

6) The model's ability to classify diseases as compared to expert radiologists (RQ6): The aforementioned experimental

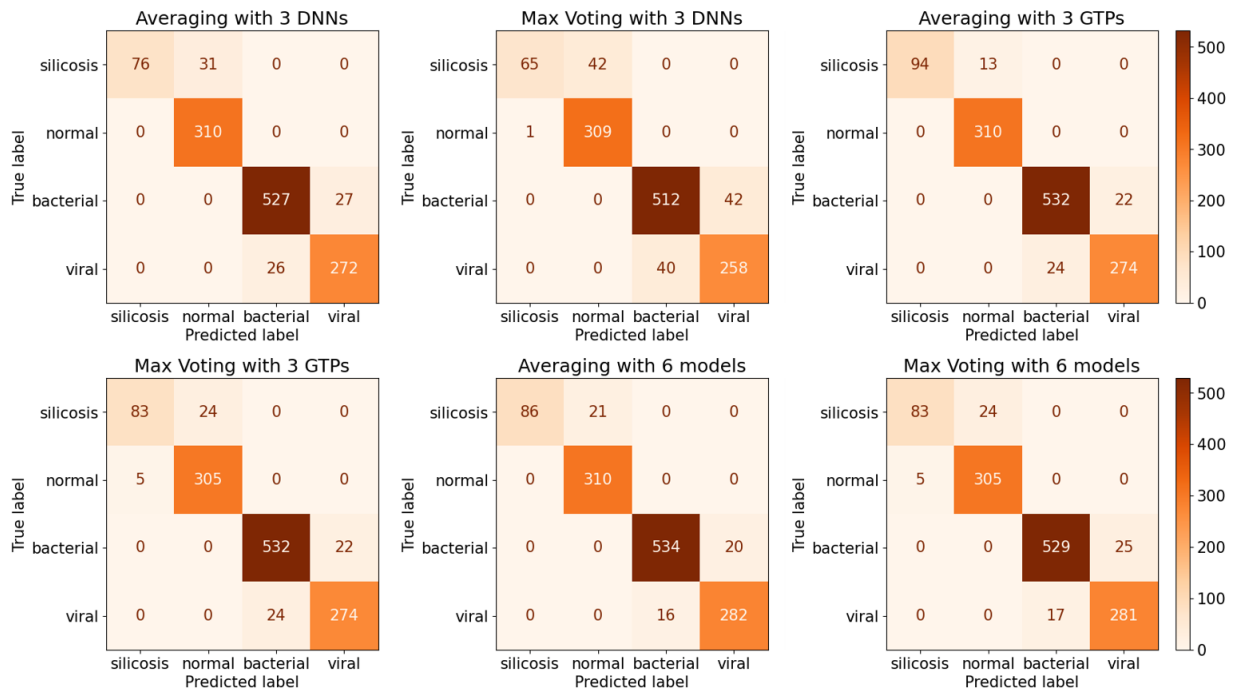


Fig. 4: The confusion matrices for the 4 classification classes correspond to 6 different ensemble cases.

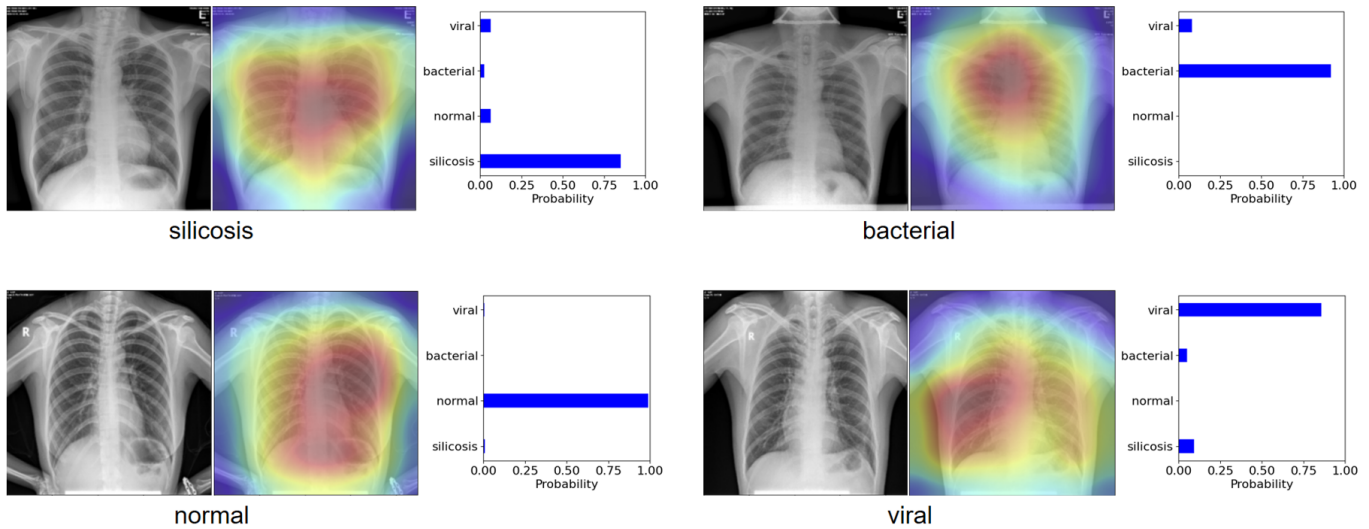


Fig. 5: The visualization of the attention maps corresponds to each image in the 4 classes and the chart represents the prediction confidence score of the DenseNet201-GTP model.

findings suggest the viability of implementing the proposed model in practical scenarios. While acknowledging the limitations of the model in fully substituting expert decision-making from a medical ethics standpoint and recognizing its current capabilities, the model is positioned as an auxiliary tool for radiologists. Nevertheless, in terms of experimentation, this section presents certain comparisons between the model’s predictions and those generated by experts.

We employ a portion of the dataset for assessment, including 107 silicosis images and 310 normal chest X-ray images. The data is evaluated by the Council of the Occupational Radiology Association for Pneumoconiosis, affiliated with

the Vietnamese Occupational Medicine Association in Thai Nguyen. The council, led by Prof. Dr. Do Van Ham, head of the Occupational Health Department, possesses over 40 years of experience in researching, teaching, and training in occupational diseases, particularly those related to lungs, bronchi, and occupational silicosis. The evaluation process is conducted in two steps: (i) reviewing the implementation of X-ray imaging according to occupational medicine technical standards, and (ii) meticulous analysis of images to accurately reflect the health status of workers. Additionally, the council conducts evaluations through two independent rounds, with the final conclusion made by the Chairman of the Council - a

		Predicted Class	
		Silicosis	Normal
Actual Class	Silicosis	40	67
	Normal	4	306

TABLE V: The confusion matrix results from the radiologists

leading professor in occupational medicine in Vietnam.

Proficiency in Categorizing Multiple Disease Classes.

From an expert standpoint, radiologists lack precise guidelines to distinctly differentiate various forms of lung inflammation (attributed to silica, bacteria, viruses, etc.). While experts can efficiently diagnose normal and diseased lungs based on abnormalities and opacities, they often encounter challenges in precisely classifying specific diseases within broader categories. In contrast, the model exhibits a relatively effective ability to predict labels for three distinct disease classes, marking a notable advantage over human experts. We hypothesize that the model may have acquired knowledge of latent features in the images—features that humans cannot infer or visually perceive with the naked eye.

Comparing Model Predictions with Expert Assessments.

Experts analyzed and evaluated the 417 images. Patient-specific details (name, age, patient code) linked to each image were withheld to maintain objectivity. Findings from Table V reveal that the models consistently outperform expert predictions in terms of classification accuracy, demonstrating noticeably reduced misclassification rates. This implies the model’s potential as an effective supportive tool for healthcare professionals.

VI. CONCLUSION AND DISCUSSIONS

In this study, we present a comprehensive approach to the classification and detection of lung inflammation, with a specific focus on silicosis and related conditions. The constructed chest X-ray dataset - SVBCX, featuring classes corresponding to different causative agents, enhances the diversity and relevance of the training data for deep learning models. The proposed model architecture, integrating a graph transformer network and employing Balanced Cross-Entropy, exhibits improved capabilities in capturing nuanced patterns across diverse classes of lung inflammation.

The ensemble of models, a key highlight of our contributions, underscores the significance of leveraging multiple architectures to amalgamate their strengths. The ensemble achieves exceptional performance metrics, with a macro-F1 score reaching 0.9749 and AUC ROC scores consistently surpassing 0.99 for all classes. These results signify the robustness and generalization capabilities of our approach in accurately classifying and detecting diverse forms of lung inflammation.

The implications of our work extend beyond the realm of medical image analysis, addressing critical occupational health concerns. The ability to detect lung inflammation, especially among workers exposed to crystalline silica dust, underscores the practical relevance of our research. As future work, we

envision further refinement of the model and exploration of its applicability in real-world clinical settings, contributing to the ongoing efforts in improving respiratory health assessment and early detection of occupational lung diseases.

REFERENCES

- [1] C. M. Barber, D. Fishwick, M. Carder, and M. van Tongeren, “Epidemiology of silicosis: reports from the sword scheme in the uk from 1996 to 2017,” *Occupational and Environmental Medicine*, vol. 76, no. 1, pp. 17–21, 2019.
- [2] L. T. T. Xuan, L. T. Huong, K. V. Duy, N. N. Anh, P. T. Quan, N. T. Thao, N. Q. Doanh, P. T. M. Huong, and T. T. K. Nhung, “Characteristics of pulmonary lesion and related factors among workers exposed to silica dust in phu yen in 2020 workers of phu yen in 2020,” *Journal of Medical Research - Hanoi Medical University*, pp. 300–307, Aug 2021.
- [3] Centers for Disease Control and Prevention (CDC), “Silicosis screening in surface coal miners—pennsylvania, 1996-1997,” *MMWR. Morbidity and Mortality Weekly Report*, vol. 49, no. 27, pp. 612–615, 2000.
- [4] R. Fernández Álvarez, C. Martínez González, A. Quero Martínez, J. J. Blanco Pérez, L. Carazo Fernández, and A. Prieto Fernández, “Guidelines for the diagnosis and monitoring of silicosis,” *Archivos de Bronconeumologia*, vol. 51, no. 2, pp. 86–93, 2015.
- [5] C. M. Jones, S. S. Pasricha, S. B. Heinze, and S. MacDonald, “Silicosis in artificial stone workers: Spectrum of radiological high-resolution ct chest findings,” *Journal of Medical Imaging and Radiation Oncology*, vol. 64, no. 2, pp. 241–249, 2020.
- [6] J. Liu, M. Li, R. R. Liu, Y. Zhu, G. Q. Chen, X. B. Li, C. Geng, J. J. Wang, Q. X. Gao, and H. Y. Heng, “Establishment of a ct image radiomics-based prediction model for the differential diagnosis of silicosis and tuberculosis nodules,” *Chinese Journal of Industrial Hygiene and Occupational Diseases*, vol. 37, no. 9, pp. 707–710, 2019.
- [7] F. R. Song, W. Qiu, B. Ruan, W. M. Zhu, G. J. Yang, L. Li, W. H. Geng, and H. Y. Zhao, “A comparative study on diagnosis of silicosis by digital and high kv film-screen chest radiography,” *Chinese Journal of Industrial Hygiene and Occupational Diseases*, vol. 38, no. 12, pp. 919–921, 2020.
- [8] S. R. Teixeira and A. Naves, “Chest x-ray: an examination that has been in use for centuries but is still essential, especially in the clinical management of newborns in the neonatal intensive care unit,” *Radiol Bras*, vol. 51, no. 1, pp. VII–VIII, 2018.
- [9] G. Tourassi, S. Voisin, V. Paquit, and E. Krupinski, “Investigating the link between radiologists’ gaze, diagnostic decision, and image content,” *Journal of the American Medical Informatics Association*, vol. 20, no. 6, pp. 1067–1075, 2013.
- [10] M. L. Giger and K. Suzuki, “Computer-aided diagnosis,” in *Biomedical Information Technology*. Academic Press, 2008, pp. 359–XXII.
- [11] Y. Lee, Y. Chae, and S. Jeon, “Integration and evaluation of clinical decision support systems for diagnosis idiopathic pulmonary fibrosis (ipf),” *Healthcare Informatics Research*, vol. 16, no. 4, pp. 260–272, 2010.
- [12] R. Najjar, “Redefining radiology: a review of artificial intelligence integration in medical imaging,” *Diagnostics*, vol. 13, no. 17, p. 2760, 2023.
- [13] S. Albahli, H. T. Rauf, A. Algosabi, and V. E. Balas, “Ai-driven deep cnn approach for multi-label pathology classification using chest x-rays,” *PeerJ. Computer Science*, vol. 7, p. e495, 2021.
- [14] R. Kundu, R. Das, Z. W. Geem, G. T. Han, and R. Sarkar, “Pneumonia detection in chest x-ray images using an ensemble of deep learning models,” *PloS One*, vol. 16, no. 9, p. e0256630, 2021.
- [15] T. B. Chandra and K. Verma, “Pneumonia detection on chest x-ray using machine learning paradigm,” in *Proceedings of 3rd International Conference on Computer Vision and Image Processing*, ser. Advances in Intelligent Systems and Computing, B. Chaudhuri, M. Nakagawa, P. Khanna, and S. Kumar, Eds., vol. 1022. Springer, 2020.
- [16] K. M. Kuo, P. C. Talley, C. H. Huang, and L. C. Cheng, “Predicting hospital-acquired pneumonia among schizophrenic patients: a machine learning approach,” *BMC Medical Informatics and Decision Making*, vol. 19, no. 1, p. 42, 2019.

- [17] H. Yue, Q. Yu, C. Liu, Y. Huang, Z. Jiang, C. Shao, H. Zhang, B. Ma, Y. Wang, G. Xie, H. Zhang, X. Li, N. Kang, X. Meng, S. Huang, D. Xu, J. Lei, H. Huang, J. Yang, J. Ji, and X. Qi, "Machine learning-based ct radiomics method for predicting hospital stay in patients with pneumonia associated with sars-cov-2 infection: a multicenter study," *Annals of Translational Medicine*, vol. 8, no. 14, p. 859, 2020.
- [18] T. Meraj, H. T. Rauf, S. Zahoor, and et al., "Lung nodules detection using semantic segmentation and classification with optimal features," *Neural Computing & Applications*, vol. 33, pp. 10737–10750, 2021.
- [19] V. Rajinikanth, S. Kadry, R. Damaševičius, D. Taniar, and H. T. Rauf, "Machine-learning-scheme to detect choroidal-neovascularization in retinal oct image," in *2021 Seventh International Conference on Bio Signals, Images, and Instrumentation (ICBSII)*, 2021, pp. 1–5.
- [20] S. Kadry, Y. Nam, H. T. Rauf, and et al., "Automated detection of brain abnormality using deep-learning-scheme: A study," in *2021 Seventh International Conference on Bio Signals, Images, and Instrumentation (ICBSII)*, 2021, pp. 1–5.
- [21] V. Rajinikanth, S. Kadry, D. Taniar, R. Damaševičius, and H. T. Rauf, "Breast-cancer detection using thermal images with marine-predators-algorithm selected features," in *2021 Seventh International Conference on Bio Signals, Images, and Instrumentation (ICBSII)*, 2021, pp. 1–6.
- [22] H. Sharma, J. S. Jain, P. Bansal, and S. Gupta, "Feature extraction and classification of chest x-ray images using cnn to detect pneumonia," in *2020 10th International Conference on Cloud Computing, Data Science & Engineering (Confluence)*, 2020, pp. 227–231.
- [23] O. Stephen, M. Sain, U. J. Maduh, and D. U. Jeong, "An efficient deep learning approach to pneumonia classification in healthcare," *Journal of Healthcare Engineering*, vol. 2019, p. 4180949, 2019.
- [24] P. Rajpurkar, J. Irvin, K. Zhu, B. Yang, H. Mehta, T. Duan, and Others, "Chexnet: Radiologist-level pneumonia detection on chest x-rays with deep learning," *ArXiv Preprint ArXiv:1711.05225*, 2017.
- [25] A. G. Taylor, C. Mielke, and J. Mongan, "Automated detection of moderate and large pneumothorax on frontal chest x-rays using deep convolutional neural networks: A retrospective study," *PloS Medicine*, vol. 15, no. 11, p. e1002697, 2018.
- [26] T. Ozturk, M. Talo, E. A. Yildirim, U. B. Baloglu, O. Yildirim, and U. Rajendra Acharya, "Automated detection of covid-19 cases using deep neural networks with x-ray images," *Computers in Biology and Medicine*, vol. 121, p. 103792, 2020.
- [27] R. E. Al Mamlook, S. Chen, and H. F. Bzizi, "Investigation of the performance of machine learning classifiers for pneumonia detection in chest x-ray images," in *2020 IEEE International Conference on Electro Information Technology (EIT)*, 2020, pp. 098–104.
- [28] J. Janizek, G. Erion, A. DeGrave, and S. Lee, "An adversarial approach for the robust classification of pneumonia from chest radiographs," in *Proceedings Of The ACM Conference On Health, Inference, And Learning*, 2020, pp. 69–79.
- [29] J. Zhang, Y. Xie, G. Pang, Z. Liao, J. Verjans, W. Li, Z. Sun, J. He, Y. Li, C. Shen, and Y. Xia, "Viral pneumonia screening on chest x-rays using confidence-aware anomaly detection," *IEEE Transactions on Medical Imaging*, vol. 40, no. 3, pp. 879–890, 2021.
- [30] T. Tuncer, F. Ozyurt, S. Dogan, and A. Subasi, "A novel covid-19 and pneumonia classification method based on f-transform," *Chemometrics and Intelligent Laboratory Systems: An International Journal Sponsored by the Chemometrics Society*, vol. 210, p. 104256, 2021.
- [31] T. Rahman, M. E. H. Chowdhury, A. Khandakar, K. R. Islam, K. F. Islam, Z. B. Mahbub, M. A. Kadir, and S. Kashem, "Transfer learning with deep convolutional neural network (cnn) for pneumonia detection using chest x-ray," *Applied Sciences*, vol. 10, no. 9, p. 3233, 2020.
- [32] G. Liang and L. Zheng, "A transfer learning method with deep residual network for pediatric pneumonia diagnosis," *Computer Methods and Programs in Biomedicine*, vol. 187, p. 104964, 2020.
- [33] A. U. Ibrahim, M. Ozsoz, S. Serte, and et al., "Pneumonia classification using deep learning from chest x-ray images during covid-19," *Cognitive Computation*, 2021.
- [34] U. Shah, A. Abd-Alrazeq, T. Alam, M. Househ, and Z. Shah, "An efficient method to predict pneumonia from chest x-rays using deep learning approach," *Studies in Health Technology and Informatics*, vol. 272, pp. 457–460, 2020.
- [35] D. Kermany, K. Zhang, and M. Goldbaum, "Labeled optical coherence tomography (oct) and chest x-ray images for classification," *Mendeley Data*, 2018.
- [36] L. Gao, L. Zhang, C. Liu, and S. Wu, "Handling imbalanced medical image data: A deep-learning-based one-class classification approach," *Artificial Intelligence in Medicine*, vol. 108, p. 101935, 2020.
- [37] Y. Shi, Z. Huang, S. Feng, H. Zhong, W. Wang, and Y. Sun, "Masked label prediction: Unified message passing model for semi-supervised classification," *Proceedings of the Thirtieth International Joint Conference on Artificial Intelligence, IJCAI 2021*, pp. 1548–1554, 2021.
- [38] Q. Jodelet, X. Liu, and T. Murata, "Balanced softmax cross-entropy for incremental learning with and without memory," *Computer Vision and Image Understanding*, vol. 225, p. 103582, 2022.
- [39] F. Leon, S.-A. Floria, and C. Bădică, "Evaluating the effect of voting methods on ensemble-based classification," in *2017 IEEE International Conference on Innovations in Intelligent Systems and Applications (INISTA)*, 2017, pp. 1–6.
- [40] A. G. Howard, M. Zhu, B. Chen, D. Kalenichenko, W. Wang, T. Weyand, M. Andreetto, and H. Adam, "Mobilenets: Efficient convolutional neural networks for mobile vision applications," *CoRR*, vol. abs/1704.04861, 2017.
- [41] G. Huang, Z. Liu, L. Van Der Maaten, and K. Q. Weinberger, "Densely connected convolutional networks," in *2017 IEEE Conference on Computer Vision and Pattern Recognition (CVPR)*, 2017, pp. 2261–2269.
- [42] Z. Liu, Y. Lin, Y. Cao, H. Hu, Y. Wei, Z. Zhang, S. Lin, and B. Guo, "Swin transformer: Hierarchical vision transformer using shifted windows," in *Proceedings of the IEEE/CVF International Conference on Computer Vision (ICCV)*, 2021.
- [43] R. R. Selvaraju, M. Cogswell, A. Das, R. Vedantam, D. Parikh, and D. Batra, "Grad-cam: Visual explanations from deep networks via gradient-based localization," in *2017 IEEE International Conference on Computer Vision (ICCV)*, 2017, pp. 618–626.



Tien Tan Nguyen was born in 1984 in Thai Nguyen, Vietnam, received her Master's degree in Computer Science from Hanoi University of Education in 2010. She is currently a lecturer in the Department of Mathematics and Informatics at Thai Nguyen University of Medicine and Pharmacy, specializing in machine learning and image processing.



BAO BUI-QUOC was born in Thai Binh, Viet Nam in 1998. He received a B.E. degree in applied mathematics and informatics from Hanoi University of Science and Technology, Ha Noi, in 2021. He is currently a Research Assistant at the College of Engineering and Computer Science, VinUniversity. His research interests include computer vision, image processing, and machine learning/reinforcement learning.



Duy Minh Le is an undergraduate student in the Faculty of Information Technology at the Post & Telecommunication Institute of Technology in Hanoi, Vietnam. His research interests include machine learning, Neuro-Symbolic AI and reinforcement learning.



ing, and machine learning.

Cong Tran received his doctoral degree in computer science from Dankook University, Yongin, Republic of Korea, in 2021. He previously received his M.Sc. in computer science in 2014 and his B.Sc. in network and communication in 2009 from Vietnam National University, Hanoi, Vietnam. Since September 2021, he has been with the Faculty of Information Technology, Posts & Telecommunication Institute of Technology, Hanoi, Vietnam, as a lecturer. His research interests include social network analysis, data min-



(PTIT) and a Visiting Research Scientist at VinAI Research. Previously, he was a Visiting Professor at the University of Palermo, Italy and a Marie Curie Research Fellow at Philips Research, Eindhoven, the Netherlands.

Cuong Pham got a B.S in Computer Science at Vietnam National University in 1998, an MS in Computer Science at New Mexico State University, USA in 2005, and a PhD in Computer Science at Newcastle University, United Kingdom in 2012. He main research interests are ubiquitous computing, wearable computing, human activity recognition, and machine learning/deep learning. Currently, Cuong Pham is an Associate Professor of Computer Science at Posts and Telecommunications Institute of Technology